Modified Cam-Clay Model for Large Stress Ranges and its Predictions for Geological and Drilling Processes

Mahdi Heidari[1†], Maria A. Nikolinakou[1†], Peter B. Flemings[2]

[1] Bureau of Economic Geology, The University of Texas at Austin

[2] Professor, Department of Geological Sciences, and Research Scientist, Institute for Geophysics; Jackson School of Geosciences, The University of Texas at Austin

Corresponding author: Mahdi Heidari (mahdiheidari@utexas.edu)

† 10100 Burnet Road, Building PRC 130, Austin, TX 78758, USA

Key points:

- The Modified Cam-Clay model is modified to include the stress dependency of the friction angle and the slope of the compression curve.
- The new model predicts the stress dependency of the mudrock behavior, including the K_0 and the undrained strength ratios.
- The stress dependency of the friction angle significantly impacts the topography of critical wedges and the stability of wellbores and channels.

Keywords: friction angle; compression curve; critical-taper theory; Modified Cam-Clay model; slope stability; drilling window; in situ stresses

Abstract

We modify the Modified Cam-Clay (MCC) model for large stress ranges encountered in geological applications. The MCC model assumes that the friction angle (ϕ) and the slope of the compression curve (λ) of a mudrock are constant and thus predicts constant values for the lateral effective stress ratio under uniaxial, vertical strain (K_0) and undrained strength ratio ($\frac{S_u}{\sigma_v'}$). However, experimental work shows that λ, ϕ, and $\frac{S_u}{\sigma_v'}$ decrease and K_0 increases substantially with stress over large stress ranges (e.g., up to 100 MPa). We incorporate the stress dependency of λ and ϕ into the MCC model and use the new model to predict $\frac{S_u}{\sigma_v'}$ and K_0 ratios. The modified model, with only one additional parameter, successfully predicts the stress dependency of these ratios. We encode the modified model and use it for finite-element analysis of a salt basin in the deepwater Gulf of Mexico. The stresses that the new model predicts around salt differ significantly from those predicted using the original model. We incorporate the stress dependency of the friction angle into the analytical models developed for critical tapers, wellbore drilling, and the stability of submarine channel levees. We show that the decrease of the friction angle with stress 1) results in a concave surface for critical wedges, 2) shifts the drilling window to higher mud weights and makes it narrower for a vertical wellbore, and 3) causes deep-seated failure of submarine channel levees at lower angles. Our study could improve in situ stress and pore pressure estimation, wellbore drilling, and quantitative understanding of geological processes.

41 **Table 1.** Nomenclature.

Symbol	Description
ρ	Bulk density of sediments
ρ_w	Density of pore water
ρ'	Bulk density of sediments minus the density of pore water
g	Gravitational acceleration
α_w	Surface angle of a critical wedge
β_w	Dipping of décollement
μ_b	Sliding friction coefficient of décollement
ϕ_b	Friction angle of décollement
ϕ	Internal friction angle at the critical state
ϕ_{mb}	Internal friction angle at critical state at stress level at the base of a wedge
H	Wedge thickness
H_0	Wedge thickness at toe
X	Horizontal distance along a critical wedge
σ'_1	Maximum effective principal stress
σ'_2	Intermediate effective principal stress
σ'_3	Least effective principal stress
σ'_m	Mean effective stress
σ'_v	Vertical effective stress
σ_v	Vertical stress
σ_1	Maximum principal stress
σ_3	Least principal stress
h	Height of a levee
α	Central angle of a failure surface in a levee
β	Angle of a levee
u	Pore pressure
u_h	Hydrostatic pressure

λ^{i}	Overpressure ratio
K_0	Ratio of horizontal to vertical effective stress under uniaxial, vertical strain
S_u	Undrained strength
$\frac{S_u}{\sigma_v^{'}}$	Undrained strength ratio
ε	Total strain tensor
ε^e	Elastic strain tensor
ε^p	Plastic strain tensor
$\sigma^{'}$	Effective stress tensor
e	Void ratio
κ	Slope of recompression line
q	Deviatoric (shear) stress
M	Secant slope of a failure envelope
$\sigma_{m0}^{'}$	Horizontal size of a yield surface
Λ	Multiplier of plastic strain increment tensor
N	Intercept of isotropic normal compression line
λ	Slope of isotropic normal compression line
$\sigma_{mcr}^{'}$	Mean effective stress at the critical (failure) state
M_0	Coefficient for the power-law failure envelope
m	Power coefficient for the power-law failure envelope
λ_0	Coefficient for the power-law isotropic normal compression curve
n	Power coefficient for the power-law isotropic normal compression curve
κ_0	Coefficient for the power-law recompression curve
$P_{collapse}$	Minimum mud pressure for limited wellbore breakout
W	Weight of failing mass in a levee
l	Leverage of weight of failing mass in a levee
R	Radius of failure surface in a levee
γ	Dipping of failure surface in a levee
z	Depth from top surface of a levee

κ_{salt}	Slope of isotropic compression line for rock salt

1. Introduction

The friction angle and the compression curve are two of the most critical rock parameters for many geological and hydrocarbon-production processes. Friction angle controls the geometry and activity of faults (Hubbert and Rubey, 1959; Suppe, 2007), the stability of earth slopes (Hubbert and Rubey, 1959; Sawyer et al., 2014; Stigall and Dugan, 2010), and the geometry of critical tapers such as in accretionary wedges and fold-and-thrust belts (Dahlen, 1990; Davis et al., 1983; Gao et al., 2018). Friction angle also impacts hydrocarbon production. It affects the ratio of horizontal to vertical effective stress under uniaxial strain (K_0) and thereby the least principal stress, which is a key control on the maximum hydrocarbon column in reservoirs (Flemings et al., 2002) and on appropriate mud pressures for drilling wellbores (Alberty and McLean, 2004). The compression curve is a central factor in basin subsidence and deposition, pore pressure prediction (Hart et al., 1995), and processing and interpretation of seismic data (Cook and Sawyer, 2015).

The friction angle and the slope of the compression curve are typically assumed to be constant in analyses of geologic processes. Examples include analytical models such as the critical-taper theory (Dahlen, 1990; Davis et al., 1983), the limit-state slope stability models (Hubbert and Rubey, 1959; Sawyer et al., 2014; Stigall and Dugan, 2010), the Earth's strength profiles (Suppe, 2014), and wellbore stability models (Zoback, 2010). Numerical analyses also typically assume these rock properties are constant (Heidari et al., 2019; Nikolinakou et al., 2018b). For example, the Modified Cam-Clay (MCC) model, a commonly used constitutive model in finite-element analyses, assumes that the critical-state friction angle and the slope of the compression curve are constant and thus predicts constant values for the K_0 stress ratio and the undrained strength ratio ($\frac{S_u}{\sigma_v'}$). The assumption of constant rock properties is based on experimental observations over small stress ranges typically encountered in geotechnical engineering practices (< 1 MPa) (Muir Wood, 1990).

Experimental tests carried out on mudrocks over large stress ranges encountered in geological settings (~ 100 MPa), however, show that the friction angle and the slope of compression curve actually vary substantially with stress. For example, Bishop et al. (1965) conducted undrained shear tests on London Clay samples that were resedimented and consolidated under isotropic stress of up to 7.5 MPa. They reported that as stress increased from low values to 6 MPa, the undrained strength ratio decreased from 0.24 to 0.2 and the friction angle decreased from 21° to 16.1°. Yassir (1989) conducted undrained shear tests on resedimented and uniaxially consolidated soils from a mud volcano in Taiwan. They reported a decrease in the friction angle from 26.1° to 22.6° when stress increased from 5 MPa to 68 MPa. Saffer and Marone (2003) made similar observations on the friction angle of illite- and smectite-rich shales; they used a biaxial shear device to measure the friction angle for a stress range of 5–150 MPa and observed that as the normal stress increased over this range, the coefficient of friction decreased from 0.30 to 0.07 for the smectitic shales and from 0.63 to 0.41 for the illitic shales. Similarly, Ikari et al. (2007) conducted biaxial shear tests at different normal stresses of up to 100 MPa on Na- and Ca-montmorillonite-based fault gouges with different water and

quartz contents and observed that the coefficient of friction in all cases decreased significantly as the normal stress increased (for more references, see Moore and Lockner (2007)). Jones (2010) conducted undrained shear tests with pre-consolidation stresses of up to 10 MPa on resedimented Ugnu Clay from Northern Alaska and reported that the friction angle decreased from 35.1° to 23.6° when stress increased from 0.2 MPa to 9.8 MPa; he also observed a decrease in the undrained strength ratio and an increase in the K_0 ratio with stress. Recently, Gaines et al. (2019) reported residual friction angles obtained from triaxial tests conducted between 2005 and 2018 on more than 300 hard-rock samples from a mine site. The confinement stress in the tests reached as high as 70 MPa. They showed that, irrespective of the rock type, the friction angle decreased significantly with the confining stress. Abdulhadi et al. (2012) and Casey et al. (2016) conducted a series of triaxial and uniaxial tests on resedimented mudrocks with a wide variety of lithology and composition for a stress range of 0.1–100 MPa. They observed that the critical-state friction angle, the K_0 ratio, and the undrained strength ratio of all mudrocks varied systematically with stress. For instance, for resedimented material from a highly plastic (liquid limit = 79%; clay fraction = 63%), smectite-rich (smectite = 87% of clay fraction) mudrock in the Eugene Island 330 field, Gulf of Mexico, (hereafter termed RGoM EI), as stress increased from 0.3 MPa to 63 MPa, the friction angle decreased dramatically from nearly 32° to 12°, the K_0 stress ratio increased from 0.55 to 0.91, and the undrained strength ratio decreased from 0.3 to 0.1 (Table 2; points, Figures 1b–d). Experimental data also show that the compression behavior of mudrocks and sands does not follow a linear trend over large stress ranges (Mesri and Olson, 1971; Pestana and Whittle, 1995; Velde, 1996). This behavior was also reported in tests conducted by Casey et al. (2019) (points, Figure 1a).

In this paper, we modify the Modified Cam-Clay (MCC) constitutive model to incorporate the stress dependency of the friction angle and the slope of the compression curve. The MCC model is the most widely used constitutive model to describe the behavior of clays and poorly lithified mudrocks because, with a minimal number of parameters, it satisfactorily represents essential mechanical characteristics of mudrocks such as dependence on the confining stress, strain hardening and softening, and the critical state (Muir Wood, 1990; Roscoe and Burland, 1968). We calibrate the new model with the friction angles and the nonlinear compression curve measured over a stress range of 0.1–100 MPa for RGoM EI mudrocks (Casey et al., 2016; Ge, 2019) and use the calibrated model to predict the K_0 ratio, undrained strength ratio, and undrained effective stress paths over a stress range of 0.1–100 MPa. We encode the new MCC model and use the code in conjunction with finite-element code Abaqus to predict stresses in a salt basin in the deepwater Gulf of Mexico. We also incorporate the stress dependency of the friction angle into analytical models developed for the topography of critical wedges, strength profiles of Earth's crust, stability of submarine channels, and appropriate drilling windows and illustrate the significance of this dependency to these processes.

Table 2. Stresses measurements from triaxial tests on resedimented mudrock samples from Eugene Island, Gulf of Mexico (RGoM EI) (Casey et al., 2016). Samples were uniaxially compressed to a certain vertical effective stress and then sheared in undrained conditions to the critical state. Samples were compressed to a large range of vertical effective stresses.

Uniaxial compression		Undrained shearing			
σ'_v	$K_0=\frac{\sigma'_h}{\sigma'_v}$	σ'_{vcr}	σ'_{hcr}	$\phi=\sin^{-1}\left(\frac{\sigma'_{vcr}-\sigma'_{hcr}}{\sigma'_{vcr}+\sigma'_{hcr}}\right)$	$\frac{S_u}{\sigma'_v}=\frac{\sigma'_{vcr}-\sigma'_{hcr}}{2\sigma'_v}$
0.126	0.619	0.090	0.034	26.9	0.222
0.333	0.68	0.206	0.078	26.7	0.192
0.372	0.649	0.248	0.108	23.2	0.188
0.379	0.626	0.312	0.132	23.9	0.237
0.38	0.595	0.281	0.109	26.1	0.226
0.878	0.655	0.680	0.300	22.8	0.216
1.959	0.698	1.640	0.798	20.2	0.215
9.759	0.805	6.970	4.316	13.6	0.136
9.797	0.844	7.023	4.241	14.3	0.142
9.885	0.828	9.968	6.654	11.5	0.168
63.47	0.917	38.215	25.149	11.9	0.103

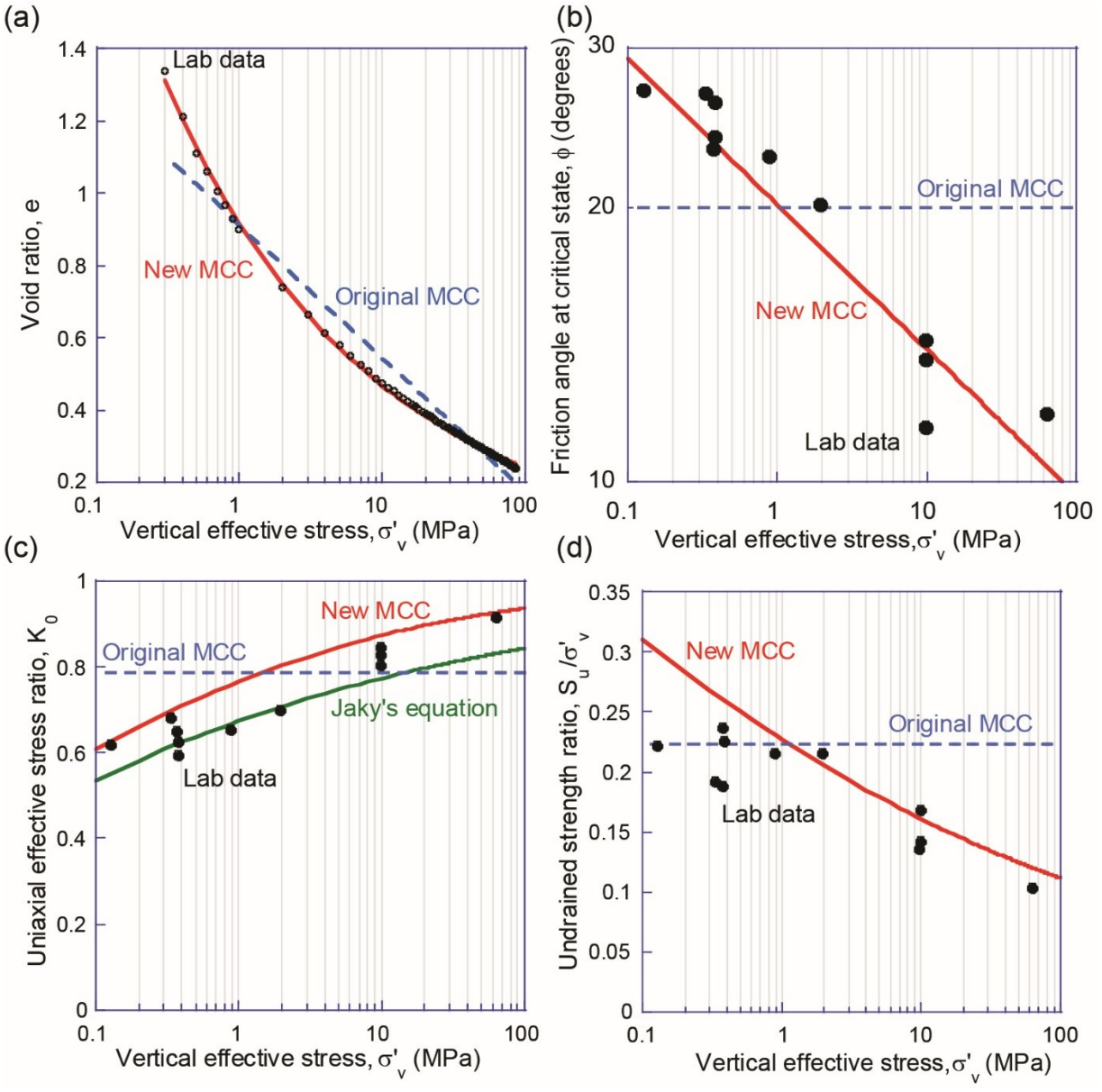

Figure 1. Measured, fitted, and predicted data for RGoM EI mudrocks over a stress range of 0.1–100 MPa. Measured data (circles) are from Casey et al. (2016) and Ge (2019). (a) Uniaxial compression. Measured data are from CRS consolidation tests. These data follow a nonlinear trend. (b) Friction angle. Both axes are in logarithmic scale. Measured data are friction angles at the critical state in undrained triaxial tests. These data show the friction angle decreases substantially with stress. (c) Uniaxial effective stress ratio (K_0). Measured data are from triaxial tests under uniaxial-strain conditions. These data show the K_0 ratio increases substantially with stress. (d) Undrained strength ratio ($\frac{S_u}{\sigma_v'}$). Measured data are based on strengths measured at the critical state in undrained triaxial tests on samples uniaxially consolidated to different vertical effective stresses. These data show the strength ratio decreases substantially with stress.

2. A stress-level-dependent MCC model

2.1 MCC model

The MCC model is an elastic-plastic model; the total strain tensor (ε) is decomposed into elastic (ε^e) and plastic (ε^p) parts:

$$\varepsilon = \varepsilon^e + \varepsilon^p. \quad (1)$$

The elastic strain is obtained from the effective stress tensor σ' using Hooke's law. The bulk modulus in this law is not constant; instead, it is assumed that the void ratio (e) changes with the logarithm of the mean stress ($\sigma'_m = \frac{\sigma'_1 + \sigma'_2 + \sigma'_3}{3}$) at a constant rate ($\kappa$) during elastic deformation:

$$de = \kappa \cdot d\left(\ln\left(\sigma'_m\right)\right), \quad (2)$$

This assumption results in a bulk modulus that increases proportionally with the mean stress. The shear modulus is either defined as an independent constant or obtained from the bulk modulus and a constant Poisson's ratio using the relationship between these parameters.

Inelastic (plastic) deformation occurs when stresses increase beyond a limit, which is characterized by the yield surface in the stress plot. This surface in the MCC model is assumed to have an elliptical form in the $q - \sigma'_m$ stress plot (dashed lines, Figure 2), in which q is the deviatoric stress ($q = \sqrt{\frac{(\sigma'_1 - \sigma'_2)^2 + (\sigma'_1 - \sigma'_3)^2 + (\sigma'_2 - \sigma'_3)^2}{2}}$):

$$f\left(\sigma'\right) = q^2 - M^2 \cdot \sigma'_m \cdot \left(\sigma'_{m0} - \sigma'_m\right) = 0, \quad (3)$$

In the MCC model, the yield surface is also used to determine plastic strains; the plastic-strain-increment tensor is assumed to be normal to the yield surface (an associated flow rule):

$$d\varepsilon^p = \Lambda \frac{\partial f(\sigma')}{\partial \sigma'} \quad (4)$$

in which variable $\Lambda \geq 0$ is a scalar function of stresses.

The MCC model follows the critical-state theory, which states that the volumetric plastic strain increment is zero at the critical (post-peak) state. Thus, the crest of the yield surface (points, Figure 2), at which the volumetric plastic strain increment vanishes (equation 4), represents the critical state (Atkinson and Bransby, 1977). Further, parameter M in equation 3, which expresses the slope of the line emanating from the origin to the crest of the yield surface, represents the secant slope of the critical-state (failure) envelope in the $q - \sigma'_m$ stress plot (solid lines, Figure 2). This parameter can be obtained from the friction angle of the rock at the critical-state (ϕ) as $M = \frac{6\sin(\phi)}{3 - \sin(\phi)}$.

168

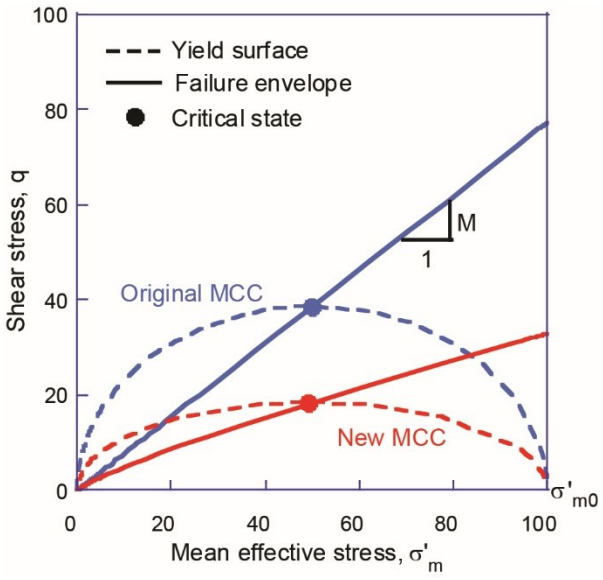

Figure 2. Yield surface and critical-state (failure) envelope in original (blue) and new (red) MCC models. In both models, the yield surface is an ellipsoid and the critical-state envelope passes through the crest of the yield surface. The failure envelope, however, is different in the two models; it is linear in the original model and curvilinear in the new model.

Stress variable σ'_{m0} in equation 3 represents the size of the yield surface (Figure 2). It also represents the stress during isotropic consolidation and is assumed to vary with the volumetric plastic strain. This variation is expressed by the isotropic normal compression curve, which describes the change in the void ratio as the isotropic stress (σ'_{m0}) increases . In the MCC model, this curve is assumed to be linear when the void ratio is plotted against the logarithm of the mean stress:

$$e = N - \lambda \cdot \ln\left(\sigma'_m\right) \quad (5)$$

in which λ is the slope and N is the intercept of the isotropic normal compression curve at $\sigma'_m = 1$.

2.2 Modification of MCC model for large stress range

We modify the failure envelope and the normal compression curve in the MCC model to incorporate the stress dependency of the friction angle and the slope of the normal compression curve (Figure 1a, b).

2.2.1 Nonlinear failure envelope

We replace the linear form of the failure envelope (solid blue line, Figure 2) with a power-law form (solid red line, Figure 2) to represent the stress dependency of the critical-state friction angle (Figure 1d):

$$q = M_0 \cdot \sigma'^{\,m}_m; \quad (6)$$

in which $q_0 > 0$ and $0 < m < 1$ are material constants. The nonlinear form of the failure envelope was envisaged in Mohr's pioneering work on failure envelopes (Holtz and Kovacs, 1981).

2.2.2 Nonlinear compression curve

We replace the linear form of the normal compression curve with a power-law form to represent the stress dependency of the slope of the compression curve (Figure 1a):

$$e = \lambda_0 \cdot \sigma_m^{'n}; (7)$$

in which $\lambda_0 > 0$ and $n < 0$ are material constants.

The power-law form in equation (7) leads to a linear relationship between $\ln(e)$ and $\ln(\sigma'_{m0})$. Pestana and Whittle (1995) studied uniaxial compression of sands with various mineralogies and showed that this linear relationship holds true for sands over large stress ranges. In contrast, Hashiguchi (1974) and Butterfield (1979) proposed a linear relationship between $\ln(1+e)$ and $\ln(\sigma'_{m0})$ to model the nonlinearity of the compression curve. We first used this relationship to develop the new MCC model (Heidari et al., 2018b). However, like the traditional linear relationship (equation 5), this relationship has a physically unacceptable property that predicts negative porosity at high stresses. Our power-law relationship (equation 7) does not have this issue, predicting zero void ratio at high stresses.

In accordance with the normal compression curve, we also replace the linear form of the elastic (unloading-reloading) compression curve with a power-law form that has the same power coefficient as the normal compression curve (n, equation 7):

$$de = \kappa_0 \cdot d\left(\sigma_m^{'n}\right); (8)$$

in which κ_0 is a constant. Experimental data indicate that the slope of the elastic compression curve decreases with stress. Thus, the linear form of the elastic compression curve, which assumes a constant slope (κ, equation 2), overestimates the swelling of rocks unloaded at high stresses (Hashiguchi, 1995). Because the slope of the elastic compression curve in our power-law form (equation 8) decreases with stress, our proposed form does not have this experimentally unacceptable property.

In the new MCC model, we modify only the failure envelope (equation 6) and the compression curves (equations 7 and 8). Other components of the MCC model, including the elliptical shape of the yield surface (equation 3) and the associativity of the flow rule (equation 4), are maintained in the new model. In Appendix A, we demonstrate that our enhancements maintain the MCC model's compatibility with thermomechanical principles.

2.3 Performance of the stress-level-dependent MCC model

We first calibrate the original and new MCC models with the same compression behavior and friction angle data for RGoM EI mudrocks over 0.1 to 100 MPa of stress (Casey et al., 2016). The available compression data are for uniaxial compression (points, Figure 1a). There is an analytical relation between isotropic and uniaxial compression parameters in the original MCC model. This relation is used to calibrate the parameters of the isotropic-compression curve in the original MCC model (λ and N, equation 5) from the uniaxial compression data. In the new

MCC model, however, there is no analytical relation between isotropic and uniaxial compression parameters; thus, we use trial and error to calibrate the parameters of the isotropic-compression curve (λ_0 and n, equation 7) from the uniaxial compression data. The power-law form proposed in the new MCC model represents the compression data points much more accurately than the linear form in the original MCC model (Figure 1a).

The parameters of the failure envelope (M_0 and m, equation 6) are determined by plotting the shear stress ($q_{cr}=\sigma'_{vcr}-\sigma'_{hcr}$) against the mean effective stress ($\sigma'_{mcr}=\frac{\sigma'_{vcr}+2\sigma'_{hcr}}{3}$) at failure that were obtained in lab tests (Table 2), and fitting a power-law function to the data points. The friction angles associated with the calibrated failure envelope fit the friction angles measured in the tests remarkably (Figure 1b). An average, constant value for friction angle, assumed in the original MCC model (dashed line, Figure 1b), obviously fails to represent the significant variation of the friction angle with stress. Tables 3 and 4 list the values of the material parameters in the original and new MCC models. These calibrated models are used to predict the K_0 ratio, the undrained strength ratio, and the undrained effective stress paths at different stress levels.

Table 3. Input parameters and their values for the original MCC model.

Parameter	Value
Secant slope of failure envelope (M)	0.772
Poisson's ratio (ν)	0.25
Intercept of isotropic normal compression line (N)	0.9
Slope of isotropic normal compression line (λ)	0.161
Slope of recompression line (κ)	0.054

Table 4. Input parameters and their values for the new MCC model.

Parameter	Value
Coefficient for power-law failure envelope (M_0)	0.712
Power coefficient for failure envelope (m)	0.832
Poisson's ratio (ν)	0.25
Coefficient for isotropic normal compression curve (λ_0)	0.89
Power coefficient for isotropic normal compression curve (n)	–0.286
Coefficient for power-law recompression curve (κ_0)	0.3

2.3.1 K_0 and $\frac{S_u}{\sigma_v'}$ ratios

The K_0 and $\frac{S_u}{\sigma_v'}$ ratios that the new MCC model predicts over the large stress range (0.1–100 MPa) vary substantially with stress (red solid lines, Figures 1c–d). The predicted values of both ratios agree satisfactorily with the experimental values (points, Figures 1c–d). The new MCC model slightly overestimates experimental values of the K_0 ratio at all stress levels. This systematic overestimation is an attribute inherited from the original MCC model. McDowell and Hau (2003) showed that this deficiency in the MCC model derives from the use of an associated flow rule (equation 4), which leads to overestimation of plastic strains. They showed that this issue can be eliminated if the MCC model is used with a non-associated flow rule. The ratios that the original MCC model predicts are constant (dashed lines, Figures 1c–d), obviously failing to represent the substantial stress dependency of the ratios.

To evaluate the role that the nonlinearity of the failure envelope and the compression curve each has in the stress dependency of the ratios, we predict K_0 and $\frac{S_u}{\sigma_v'}$ ratios for a constant friction angle and a nonlinear compression curve. Values that are obtained for the ratios are constant and identical to those obtained from the original MCC model, illustrating that the nonlinearity of the compression curve contributes neither to the magnitude nor to the stress dependency of these ratios.

The MCC model is not the only approach used to predict the K_0 ratio. The K_0 ratio in the MCC model is obtained by combining all the model equations and solving them for zero lateral strains; as a result, the ratio that this model predicts depends on all properties of the material (Table 3). Several empirical relationships have been suggested to estimate this ratio simply as a function of only the friction angle (e.g., Brooker and Ireland, 1965; Mesri and Hayat, 1993). Among these relationships, Jaky's equation, $K_0 = 1 - \sin(\phi)$, is the most widely used (Jaky, 1948; Mayne and Kulhawy, 1982). Like the MCC model, these relationships assume that the friction angle is constant. We test the Jaky's relationship to predict the K_0 ratio for RGoM EI mudrocks over the vertical effective stress range of 0.1–100 MPa, considering the stress dependency of the friction angle. We crossplot the friction angles measured in lab tests on RGoM EI mudrocks (ϕ, Table 2) against the consolidation vertical effective stress in the tests (σ_v', Table 2) and then fit a power-law curve to the resulting data points. For any given vertical effective stress, we use this curve to calculate the friction angle for Jaky's equation to calculate the K_0 ratio. The K_0 ratios that Jaky's equation produces (green line, Figure 1c) vary with stress and satisfactorily predict the measured K_0 ratios at low stresses but underestimate this ratio at high stresses.

2.3.2 Effective-stress paths in undrained conditions

Porosity of a rock is constant during an undrained test. Therefore, the effective-stress path in an undrained test constitutes effective stresses that the rock can have for a certain porosity. Effective-stress paths have thus found a key role in modern porosity-based prediction of pore pressure in subsurface mudrocks (Flemings and Saffer, 2018; Goulty, 2004; Hauser et al., 2014; Heidari et al., 2018a).

Casey et al. (2016) conducted undrained triaxial tests on RGoM EI mudrocks pre-consolidated under uniaxial-strain conditions to different vertical effective stresses. We show the effective-stress path in two of these tests, one at a low pre-consolidation stress of $\sigma_v^{'}=0.356$ MPa (dashed line, Figure 3a) and one at a high pre-consolidation stress of $\sigma_v^{'}=63.47$ MPa (dashed line, Figure 3b). Each path begins at a uniaxial-strain (K_0) stress state (solid points, Figure 3) and ends at the critical (shear failure) state (hollow points, Figure 3). We use the original and new MCC models to predict the effective-stress paths in these two tests. At both stress levels, the new MCC model predicts the effective-stress path (green solid line, Figure 3a; red solid line, Figure 3b) more accurately than the original MCC model (blue lines, Figure 3a, b). This is in part due to the fact that the new model predicts the beginning and the end points of the paths more accurately. This is because the location of the beginning points (solid circles, Figure 3)—representing uniaxial-strain pre-consolidation—is a function of the K_0 ratio, and the location of the end points (hollow circles, Figure 3)—representing the critical state—is a function of the $\frac{S_u}{\sigma_v^{'}}$ ratio, and these ratios are more accurately predicted by the new MCC model than the original model at the two stress levels (Figures 1c–d).

We display the effective-stress paths in a normalized-stress plot to illustrate the effect of the mudrock's stress-level-dependent behavior on its effective-stress paths. The effective-stress paths predicted by the original MCC model map into a single, stress-level-independent path (blue line, Figure 3c) (Muir Wood, 1990). The stress paths predicted by the new MCC model, however, map into different, stress-level-dependent paths. The stress path at low stress levels (green solid line, Figure 3c) is larger than the path predicted by the original MCC model (blue line, Figure 3c). However, as stress level increases, the stress path becomes progressively smaller, even smaller than the path predicted by the original MCC model at high stress levels (red solid line, Figure 3c).

2.4 Limitations of the new MCC model

Like the original MCC model, the new MCC model describes the intrinsic behavior of mudrocks (Burland, 1990; Fearon and Coop, 2000) and thus does not account for natural features developed in mudrocks over time such as structure (Liu and Carter, 2002; Suebsuk et al., 2010), cementation (Nguyen et al., 2014), and/or anisotropy (Rouainia and Muir Wood, 2000; Whittle and Kavvadas, 1994). These features are commonly accounted for with additional components to the MCC model. Similar components can be added to our model to account for natural features.

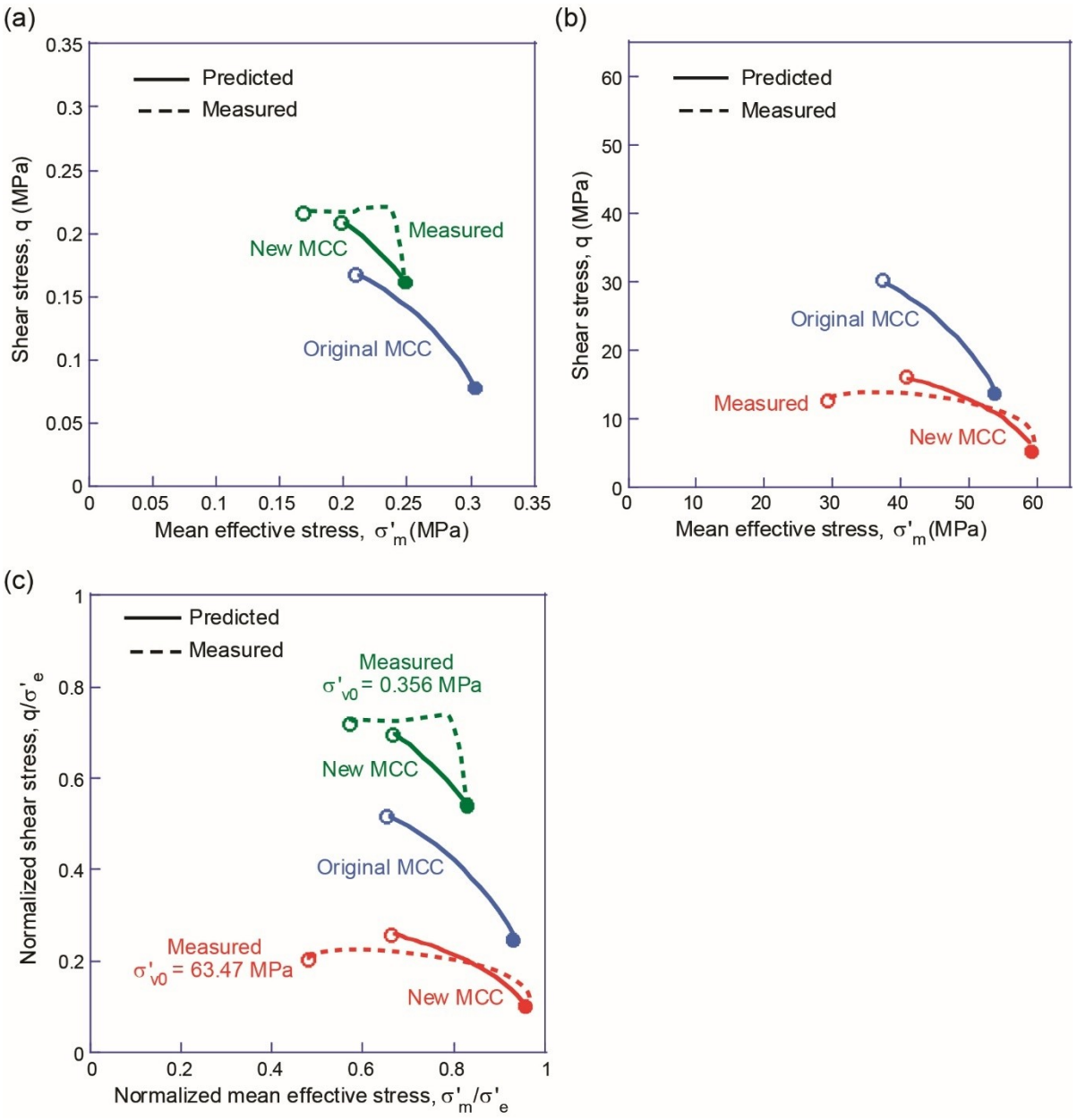

317

318 **Figure 3**. Measured effective-stress paths in undrained triaxial tests (dashed lines) vs. those
319 predicted by original (blue line) and new (green and red solid lines) MCC models. Measured
320 paths are for RGoM EI mudrocks (Casey et al., 2016) (a) at a low pre-consolidation stress of
321 $\sigma_v^{'}$=0.356 MPa; (b) at a high pre-consolidation stress of $\sigma_v^{'}$=63.47 MPa; and (c) at both stress
322 levels with stresses normalized by the equivalent stress ($\sigma_e^{'}$), which is the horizontal intercept of
323 the paths. The original MCC model produces a single, stress-level-independent path for both
324 stress levels, thereby failing to predict the stress-level-dependent measured paths. In contrast, the
325 new MCC model produces stress-level-dependent paths that successfully predict the measured
326 paths.

3. Geological applications

We discuss the impacts of the friction angle's stress dependency on a range of geological and drilling processes. We study the topography of critical wedges, appropriate drilling mud weights, the Earth's strength profile, and the stability of levees in submarine channels. Analytical models that assume a constant friction angle for mudrocks have been developed for these processes. We revisit and modify these models for a mudrock with a stress-dependent friction angle. The modified models are calibrated for RGoM EI mudrocks and used to quantitatively illustrate the impacts of the friction angle's stress dependency on the chosen processes. Lastly, we encode the new MCC model and use it in conjunction with a finite-element model to estimate stresses in a salt basin in the Gulf of Mexico.

3.1 Topography of critical wedges

The fold-and-thrust belts and submarine accretionary wedges that lie along compressive plate boundaries are one of the most recognized features of the Earth's crust (Dahlen, 1990; Gao et al., 2018; Kearey et al., 2009; Moore and Vrolijk, 1992; Saffer and Tobin, 2011; Stern, 2002). The bases of these regions, typically detachments or décollement faults, commonly dip opposite to the region's surface, resulting in a wedge-shaped cross section (Figure 4a). Subduction of the plate below a critical wedge imposes frictional drag on the wedge along its base, causing significant lateral deformation in the wedge as recorded by elevated porosity loss and abundant imbricate thrust faults and folds.

The critical-taper theory is the most widely used model to understand the mechanics of critical wedges and to quantitatively assess their geometry (Dahlen, 1990; Davis et al., 1983). This model assumes that the lateral drag imposed by the subducting plate on the wedge brings sediments within the wedge to the Coulomb frictional failure. Based on this assumption, the wedge angle ($\alpha_w+\beta_w$, Figure 4a) is at a critical, maximum value. Davis et al. (1983) used equilibrium equations and derived equations to estimate the wedge angle for a thin-skinned critical wedge of rocks with a constant friction angle. Dahlen (1990) and Skarbek and Rempel (2017) improved these equations for wedges with spatially varying (heterogeneous) properties. We use these equations and derive the equation for the angle of a wedge with a stress-dependent friction angle. For a wedge with hydrostatic pore pressure, this angle is

$$\alpha_w+\beta_w=\frac{dH}{dX}=\frac{1-\sin\left(\phi_{mb}\right)}{1+\sin\left(\phi_{mb}\right)}\left(\beta_w+\mu_b\right);(9)$$

in which ϕ_{mb} is the friction angle of the rocks within the wedge at the stress level that exists at the base of the wedge. H is the wedge thickness, which varies with distance from the toe of the wedge (X). The sliding friction coefficient of the décollement¿) can be expressed as $\mu_b=\tan\left(\phi_b\right)$, in which ϕ_b is the Coulomb friction angle for sliding at the décollement. In general, the décollement must be frictionally weaker than adjacent rocks for slip to occur there. If pore pressure in the décollement is the same as that in adjacent rocks, then $\phi_b\leq\phi_{mb}$ (e.g., Davis et al., 1983). Equation 9 is the same as the equation for the angle of a wedge with a constant friction angle φ (see equation 16 in Dahlen (1990)) if φ is replaced with φ_{mb}.

We use equation 9 to calculate the angle of a thin-skinned submarine (accretionary) wedge composed of RGoM EI mudrocks and under hydrostatic pore pressure. The décollement

has a dip (β_w) of 6° and a constant sliding friction coefficient (μ_b) of 0.12. The bulk density of mudrocks in the wedge (ρ) is 2.4 g/cm^3, and the density of pore water (ρ_w) is 1.0 g/cm^3. We first calculate the friction angle ϕ_{mb} along the wedge. Given the hydrostatic pore pressure in the wedge, the vertical effective stress at the base of the wedge is: $\sigma_v^{'}=(\rho-\rho_w)gH$, in which g is the gravitational acceleration, and H is the wedge thickness. In a thin-skinned critical wedge, $\sigma_v^{'}$ is the least effective principal stress. Accordingly, we describe the measured friction angles of RGoM EI mudrocks as a function of the least principal stress. The friction angle measured at each stress level (ϕ, Table 2) is cross plotted against the least effective principal stress at that stress level ($\sigma_{hcr}^{'}$, Table 2) in a log-log plot (circles, Figure 4b), and the resulting data points are then fitted with a line (red line, Figure 4b). This curve is used with the $\sigma_v^{'}$ calculated for the wedge base to calculate ϕ_{mb}.

Because ϕ_{mb} is a function of the wedge thickness (H), equation 9 does not yield the wedge angle directly. Instead, it is a first-order differential equation for the wedge thickness as a function of the distance along the wedge, $H(X)$. We integrate this equation numerically to find $H(X)$ and then to find the wedge angle ($\frac{dH}{dX}$) along the wedge. Accretionary wedges typically start with a thickness of a few hundred meters at the toe (H_0, Figure 4a) (e.g., 700 m in Java (Kopp et al., 2009); ~400 m in the Muroto transect of the Nankai trench (Brown et al., 2003); ~1250 m in Sumatra (Hüpers et al., 2017); and ~200 m in the Barbados (Screaton and Ge, 2000)). In our calculations, we assume H_0 = 500 m.

The stress dependency of the friction angle results in a wedge angle that increases with distance from the toe of the wedge (red α_w, Figure 4c), resulting in a concave topographic surface for the wedge (Figure 4a). This is because as distance from the toe of the wedge increases, the overburden stress at the base of the wedge increases following the increase in the wedge thickness and the friction angle at the base thus decreases (ϕ_{mb}, Figure 4c), resulting in a wedge angle that increases distancing from the wedge toe (equation 9). The slope of the wedge surface changes at a rapid rate near the toe and at a much slower rate away from the toe (Figure 4a; red α_w, Figure 4c), reflecting rapid change of friction angle at low stresses near the toe and its slow change at high stresses far from the toe (ϕ_{mb}, Figure 4c). If a constant, average friction angle (blue dashed line, Figure 4b) was assumed for the wedge mudrocks, a constant and significantly lower surface angle (blue dashed line, Figure 4c) would be predicted.

Our prediction of a concave profile for the wedge surface agrees with the finding of Dahlen et al. (1984), who predicted this profile for critical wedges with rocks that have cohesion in addition to friction angle. This agreement derives from the fact that the Mohr failure envelope of rocks with a stress-dependent friction angle is a curvilinear curve (red solid line, Figure 2) that can be approximated by a tangent linear envelope with cohesion.

Natural examples of critical wedges with concave surfaces are scarce. One reason could be that the change in the predicted surface angle (red α_w, Figure 4c) along the wedge is not larger than the margin of error for the measurement of this angle (Dahlen et al., 1984). Another reason could be that the surface concavity is canceled out or even reversed by other processes that produce convexity of the wedge surface. Examples of these processes include increase in rock cohesion due to lithification or decrease in overpressure with distance from the toe of the wedge (Zhao et al., 1986) and decrease in porosity with depth (Breen and Orange, 1992).

There are abundant examples of concave listric normal faults in extensional settings. The concavity of these faults can be explained by the stress dependency of the friction angle. In extensional settings, the maximum principal stress is vertical and the least principal stress is horizontal, thus, faults have a dip angle of $45^o+\phi/2$. In rocks with a stress-dependent friction angle, the friction angle decreases with stress (Figure 1b) and thus with depth. Because of this decrease, the dip of normal faults decreases with depth, resulting in a concave profile for faults.

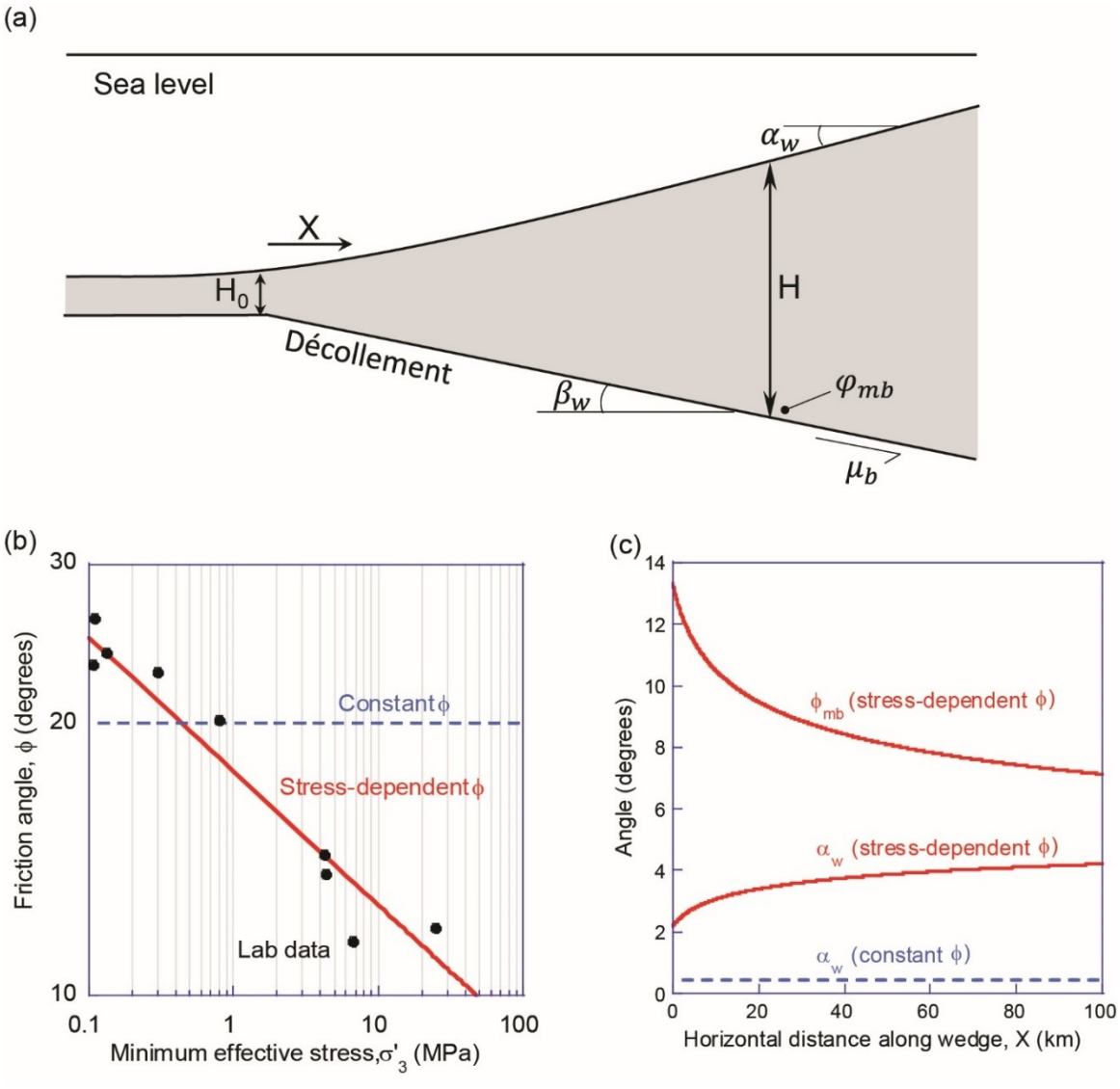

Figure 4. Topography predicted for a critical accretionary wedge composed of mudrocks with stress-dependent friction angle. (a) Schematics of the wedge. (b) Friction angle of mudrocks within the wedge as a function of the least effective stress. Both axes are in logarithmic scale. Lab data are for RGoM EI mudrocks (Casey et al., 2016). Red line represents the line fitted to lab data. (c) Friction angle of mudrocks at the stress level at the base of the wedge (ϕ_{mb}) and the predicted surface angle (red α_w) along the wedge where the wedge thickness > 500 m (H_0 = 500

m in sub-figure a). Blue dashed line is the surface angle that a constant, average friction angle (blue dashed line, subfigure b) would predict.

3.2 Appropriate drilling mud-weights

It is common practice to maintain the pressure of drilling mud in the open (uncased) section of a wellbore to be less than the least principal stress in the surrounding formation (σ_3). This practice limits outflow of drilling mud into formations due to extensive hydraulic fracturing and consequently loss of the drilling mud. The least principal stress in a formation consolidated under purely vertical, uniaxial strain is

$$\sigma_3 = K_0 \cdot \sigma_v^{'} + u \quad (10)$$

in which $\sigma_v^{'}$ is the vertical effective stress and u is pore pressure. It is also common practice to maintain the pressure of the drilling mud higher than a minimum pressure ($P_{collapse}$) to prevent excessive breakout of wall rocks (Willson and Fredrich, 2005; Zoback, 2010). If no drainage occurs in wall rocks during drilling of a wellbore (undrained conditions), the collapse pressure ($P_{collapse}$) for a vertical wellbore in a uniaxially-consolidated formation is (Kirsch, 1898)

$$P_{collapse} = \sigma_3 - S_u, \quad (11)$$

in which S_u is the undrained strength. Mud pressures between σ_3 and $P_{collapse}$ are thus appropriate pressures for drilling.

We calculate σ_3 and $P_{collapse}$ along a vertical wellbore in a formation composed of RGoM EI mudrocks and consolidated uniaxially under hydrostatic pore pressure with and without considering the friction angle's stress dependency (Figure 1b). To calculate σ_3 for a given depth, we calculate the vertical effective stress ($\sigma_v^{'}$) at that depth by subtracting hydrostatic pore pressure (u_h) from the overburden stress (σ_v) ($\sigma_v^{'} = \sigma_v - u_h$). The calculated $\sigma_v^{'}$ is then used in the K_0-$\sigma_v^{'}$ relationship for RGoM EI mudrocks (red solid line, Figure 1c) to calculate K_0 (red solid line, Figure 5a). The calculated K_0 and $\sigma_v^{'}$ are used in equation 10 to calculate σ_3. The calculated σ_3 is shown along the wellbore in Equivalent Mud Weight, $EMW\,(ppg) = \frac{\sigma_3\,(MPa)}{Depth\,(km)} \times 0.85$ (red solid line, Figure 5b), which is a common way to illustrate this stress in wellbore drilling. To calculate $P_{collapse}$ for a given depth, the calculated $\sigma_v^{'}$ for that depth is used in the $\frac{S_u}{\sigma_v^{'}}$-$\sigma_v^{'}$ relationship for RGoM EI mudrocks (solid line, Figure 1d) to calculate $\frac{S_u}{\sigma_v^{'}}$ ratio and, hence, S_u by multiplying the ratio by $\sigma_v^{'}$. The calculated S_u and σ_3 are used in equation 11 to calculate $P_{collapse}$, which is shown along the wellbore in Equivalent Mud Weight, $EMW\,(ppg) = \frac{P_{collapse}\,(MPa)}{Depth\,(km)} \times 0.85$ (red dashed line, Figure 5b). We also calculate σ_3 and $P_{collapse}$ along the wellbore (blue lines, Figure 5b) for the case in which a constant, average value is

chosen for the friction angle of the mudrocks (dashed line, Figure 1b). The K_0 and $\frac{S_u}{\sigma_v'}$ ratios in this case are constant along the wellbore (blue lines, Figure 5a). Approximating the stress-dependent friction angle with a constant, average value results in the following:

1) Underestimation of the K_0 ratio (blue solid line, Figure 5a) and the least principal stress (σ_3) (blue solid line, Figure 5b) at non-shallow depths. Because a constant friction angle does not capture the decrease of the friction angle with stress (Figure 1b), the K_0 ratio that it produces underestimates this ratio at high stresses (Figure 1c) at non-shallow depths, leading to underestimation of the least principal stress at these depths (equation 10).

2) Overestimation of the $\frac{S_u}{\sigma_v'}$ ratio (blue dashed line, Figure 5a) and the difference ($\sigma_3 - P_{collapse}$) (blue shaded area, Figure 5b) at non-shallow depths. Because the constant friction angle does not capture the decrease of the friction angle with stress (Figure 1b), the $\frac{S_u}{\sigma_v'}$ ratio that it produces overestimates this ratio and thus the undrained strength (S_u) at high stresses (Figure 1d) at non-shallow depths. Because the difference ($\sigma_3 - P_{collapse}$) equals the undrained strength (S_u) (equation 11), this leads to overestimation of this difference at these depths.

Approximating the friction angle with a constant, average value thus leads to underestimating the magnitude of appropriate mud weights and overestimating the range of these mud weights (shaded areas, Figure 5b).

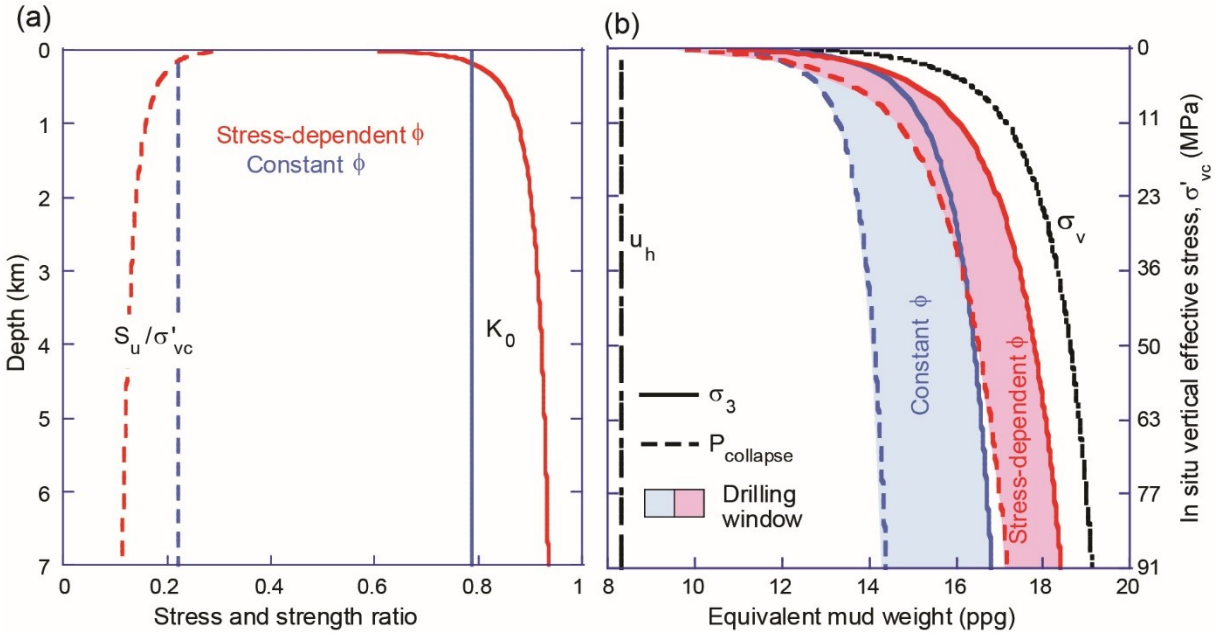

Figure 5. Stress and strength ratios and appropriate mud weights predicted along a vertical wellbore with and without considering the stress dependency of the friction angle. (a) Stress ratio

(K$_0$) and undrained strength ratio ($\frac{S_u}{\sigma_v'}$) over depth. (b) The least principal stress (σ_3), minimum mud pressure necessary for wellbore stability ($P_{collapse}$), and appropriate mud weights (drilling window) over depth. u_h = hydrostatic pressure, σ_v = lithostatic stress.

3.3 Stability of submarine channel systems

Rotational, deep-seated levee failure is common in submarine channels (Bohn et al., 2012; Jobe et al., 2011; Sawyer et al., 2014; Winker and Shipp, 2002). These failures cause large volumes of sediments to fail from channel levees into the channel, significantly affecting the form and function of the channel-levee system.

Gibson and Morgenstern (1962) and later Hunter and Schuster (1968) analyzed the circular failure of submarine levees. Consider a mass in a levee delineated by a circular cut through the levee (Figure 6a). The moment that the weight of the mass produces around the center of the circular cut (**W**·l, Figure 6a) drives the down-slope rotational failure of the mass. This failure is resisted by the moment that the shear strength of the rocks along the circular cut produces ($\int_0^{2\alpha} S_u R^2 d\theta$, Figure 6a). The stability of a levee is controlled by a mass that has the lowest ratio of resisting to driving moments. This lowest ratio is called the safety factor of the levee. In this analysis, a levee is stable if its safety factor is greater than one, unstable if its safety factor is less than one, and at the verge of failure if its safety factor is one.

Gibson and Morgenstern (1962) and Hunter and Schuster (1968) calculated the safety factor for levees with a constant strength ratio ($\frac{S_u}{\sigma_v'}$) and hydrostatic pore pressure. We revisit their analysis for levees with overpressure and stress-dependent strength ratio. In a levee with angle β and height h (Figure 6a), assuming that the rocks of the levee have consolidated uniaxially and have a uniform overpressure ratio ($\lambda^{¿} = \frac{u - u_h}{\sigma_v - u_h}$), we obtain the ratio of driving to resisting moments for a mass with angles α and γ (Figure 6a) as

$$\frac{3\left(1-\lambda^{¿}\right)\int_0^{2\alpha} \frac{S_u}{\sigma_v'} z\, d\theta}{hG(\alpha,\gamma,\beta)}, for\ 0<\gamma<\beta \wedge 0<\alpha<\frac{\pi}{2} \quad (12)$$

in which $G(\alpha,\gamma,\beta) = \sin^2\alpha \sin^2\gamma\ \ [1 - 2\cot^2\beta + 3(cot\gamma\ cot\beta + cot\gamma\ cot\alpha - cot\alpha\ cot\beta)¿$, and z is depth from the updip surface of the levee (Figure 6a). To find the safety factor of a levee, the ratio in equation 12 is calculated for different circular surfaces (different angles α and γ, Figure 6a). The surface that results in the lowest ratio is the critical surface, and the resulting ratio is the safety factor of the levee.

We use equation 12 to analyze deep-seated rotational failures in the levees of submarine channels in the Ursa Basin, Gulf of Mexico (Sawyer et al., 2014), with and without considering the friction angle's stress dependency. In these levees, β = 10°, h = 275 m, and ρ = 2 g/cm^3. We

use the friction angles of RGoM EI mudrocks for these levees, assuming that mudrocks in the two regions of the Gulf of Mexico (Ursa Basin and Eugene Island) have similar friction angles.

Because these levees have experienced failure, their safety factor at the time of failure must have dropped to one. We use this to back-calculate the overpressure ratio (λ^{*}) in these levees at the time of failure. If the friction angle is assumed to be constant, the maximum angle at which the levee is stable can be described as a function of the reduced undrained strength ratio ($\frac{S_u}{\sigma_v'}(1-\lambda^{*})$) (Figure 6b). Given the angle of Ursa Basin levees at failure (β = 10°), a reduced undrained strength ratio of 0.09 is obtained (circle, Figure 6b). The undrained strength ratio for RGoM EI mudrocks, assuming a constant friction angle, is $\frac{S_u}{\sigma_v'}$ = 0.223 (dashed line, Figure 1d). For these ratios, the overpressure ratio is obtained as λ^{*} = 0.6.

If the stress dependency of the friction angle is considered (solid line, Figure 1b), a lower overpressure ratio of λ^{*} = 0.54 is obtained. This is because our analysis in this case considers the decrease of the undrained strength ratio with stress (solid line, Figure 1d), and as a result, the rock strength is lower than assumed in the model with the constant friction angle at non-shallow rocks (dashed line, Figure 1d). Thus, we predict that the levees failed at a lower overpressure ratio than estimated by models that assume a constant friction angle (e.g., Sawyer et al., 2014).

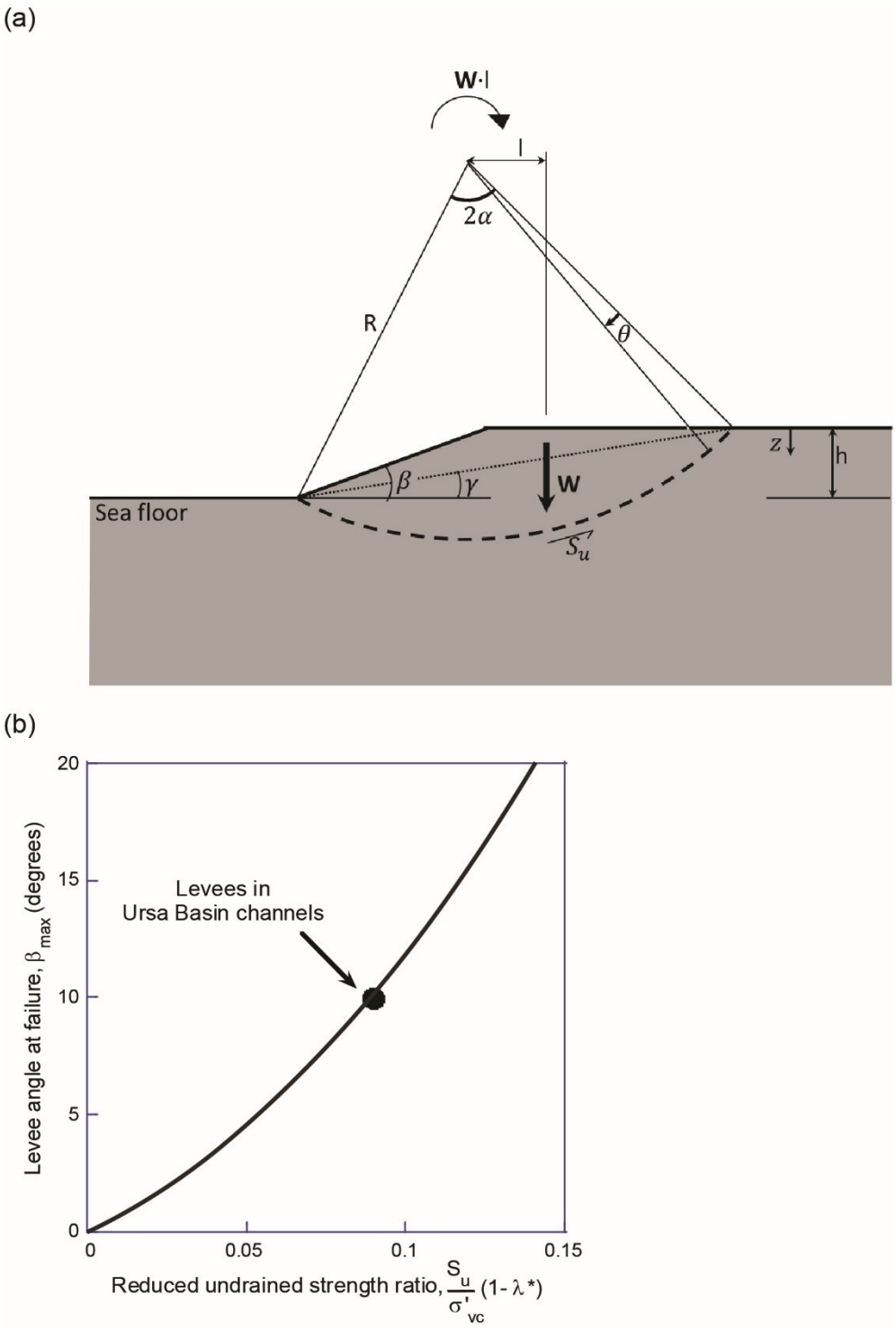

Figure 6. Stability of a submarine levee against deep-seated rotational failure. (a) Schematics of slope and circular failure surface. Weight of failing mass (**W**) drives down-slope rotation of the mass, and shear strength of rocks (S_u) along the failure surface resists this rotation. (b) Levee angle at failure as a function of reduced undrained strength ratio for rocks with a constant friction angle.

3.4 Strength profile of Earth's crust

According to the Mohr–Coulomb theory, the difference between the maximum principal stress (σ_1) and the least principal stress (σ_3) in rocks cannot exceed the rock strength:

$$\sigma_1 - \sigma_3 \leq \frac{2\sin(\phi)}{1+\sin(\phi)}\sigma_1', \quad (13)$$

in which σ_1' is the maximum effective principal stress. The strength of rocks is used to constrain in situ stresses in the Earth's crust (Suppe, 2014; Zoback et al., 1993).

Estimates of rock strength are available along a wellbore in the Brazos area, offshore Texas, Gulf of Mexico (Xiao et al., 1991). We predict the rock strength along the wellbore with and without considering the stress dependency of the rock friction angle and compare the predicted strengths to the available estimates.

The rock strength estimates (hollow circles, Figure 7c) are based on leak-off tests carried out at several depths along the well (Xiao et al., 1991). These tests provide an estimate of the least principal stress (σ_3). The estimated σ_3 are subtracted from the overburden stress (σ_1) to calculate the stress difference ($\sigma_1 - \sigma_3$). Because the well lies in a region of active normal faults, the calculated stress differences are inferred to equal the rock strength.

Equation (13) is used to predict the rock strength along the wellbore. At any given depth along the wellbore, the maximum effective principal stress (σ_1') is calculated by subtracting pore pressure from the overburden stress ($\sigma_1' = \sigma_v - u$). Suppe (2014) obtained overburden stress (σ_v) by integrating the bulk density of overburden rocks and pore pressure (u) from sonic logs along the wellbore (Figure 7b). The estimated pore pressure is almost hydrostatic above a well-defined depth and increases almost parallel to the lithostatic gradient below this depth (solid line; Figure 7b); as a result, σ_1' increases above the overpressure-onset depth and is approximately constant below this depth (dashed line, Figure 7b).

We use the friction angle of RGoM EI mudrocks in equation (13), assuming that the friction angles of mudrocks in the two regions of the Gulf of Mexico (Brazos and Eugene Island) are similar. Because σ_1' is known along the well, we describe the friction of the mudrocks (Table 2) as a function of σ_1'. Friction angles measured in the experimental tests are cross plotted against the maximum effective principal stress in the tests (Table 2) in a log-log plot (circles, Figure 7a), and then a line (red solid line, Figure 7a) is fitted to the data points. This function is used with the calculated σ_1' along the wellbore (dashed line, Figure 7b) to calculate the friction angle at any given depth along the wellbore.

If a typical, low-stress, constant value is used for the friction angle (e.g., ϕ = 24°; green dashed line, Figure 7a), the predicted strengths are a constant factor of σ_1' (equation 13); therefore, they increase linearly above the overpressure-onset depth and remain constant below this depth (green dashed line, Figure 7c). The predicted strengths disagree with the available rock strength estimates along the wellbore (hollow circles, Figure 7c). In contrast, if the stress dependency of the friction angle is considered (red solid line, Figure 7a), the predicted strengths are variable factors of σ_1' (equation 13); therefore, they increase nonlinearly above the overpressure-onset depth (red solid line, Figure 7c). Considering the stress dependency of the

570 friction angle substantially improves predictions of rock strength. The small discrepancy between
571 the predicted and estimated rock strengths (red solid line vs. points, Figure 7c) could be from a
572 possible difference between the friction angles of mudrocks at the wellbore site (Brazos) and the
573 RGoM EI mudrocks. Such a difference could be due to possible differences in lithology between
574 these two mudrocks or due to their intact versus resedimented states.
575

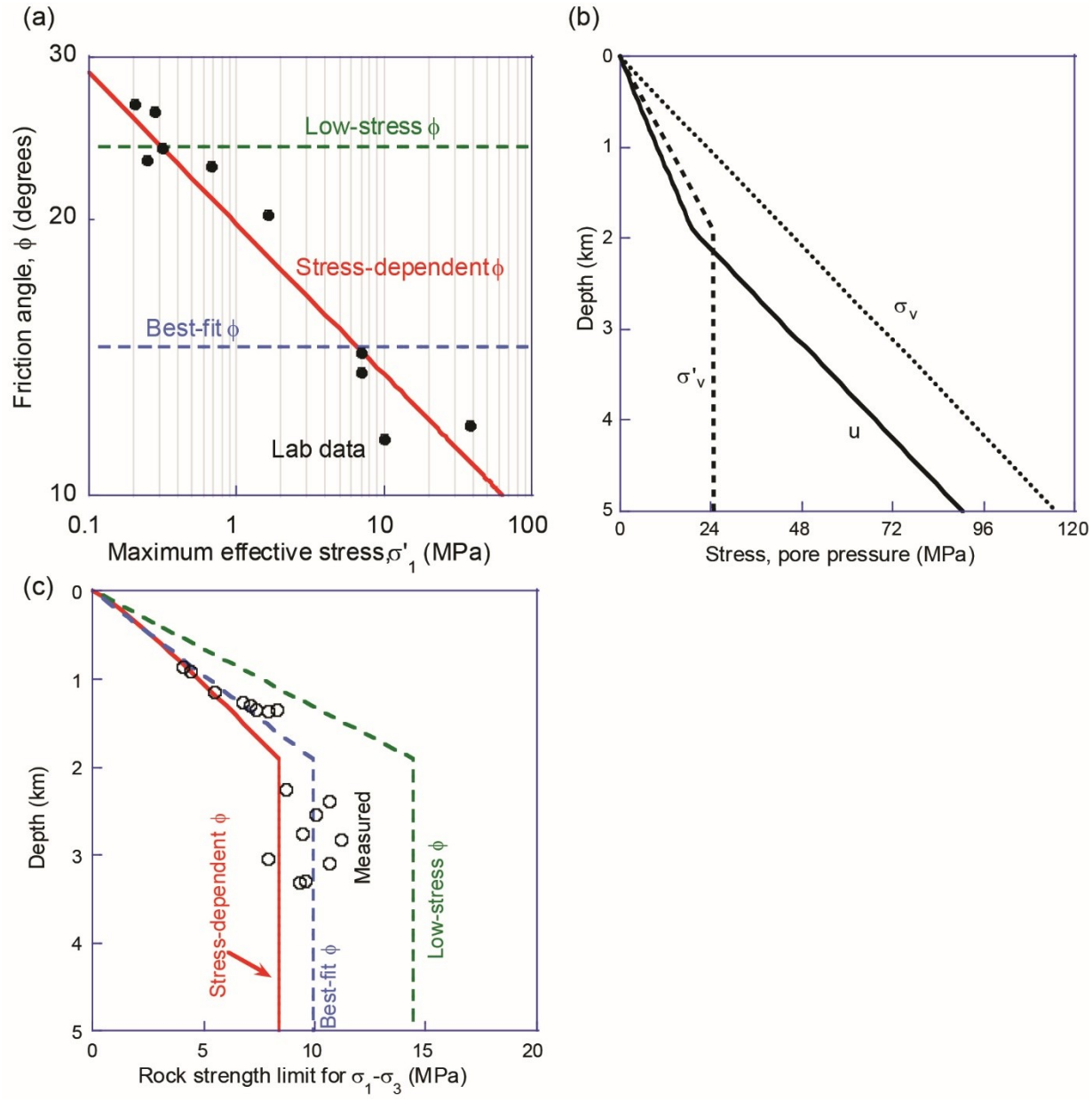

576

577 **Figure 7**. Earth strength profiles predicted along a wellbore in offshore Texas, Gulf of Mexico
578 (Suppe, 2014; Xiao et al., 1991), with and without considering the stress dependency of the
579 friction angle. (a) Friction angle as a function of maximum effective principal stress. Both axes
580 are in logarithmic scale. Lab data are for RGoM EI mudrocks (Casey et al., 2016). (b) Pore
581 pressure, lithostatic stress, and vertical effective stress over depth (modified after Suppe (2014)).
582 Pore pressure was estimated from the sonic velocity log. (c) Predicted earth strength profiles

(lines) vs. strengths estimated from leak-off tests (hollow circles) (modified after Suppe (2014)). Green line represents rock strengths predicted by a typical, constant, low-stress friction angle of 24°. Blue line represents rock strengths best fit to available data (hollow circles) and predicted by a constant friction angle. Red line represents rock strengths predicted by the stress-dependent friction angle of RGoM EI mudrocks.

We also find the constant friction angle that provides the best fit (blue dashed line, Figure 7c) to the estimated rock strengths (hollow circles, Figure 7c). This friction angle (ϕ= 14°; blue dashed line, Figure 7a) is markedly lower than typical values used for the friction angle of mudrocks (e.g., ϕ= 24°). Previous studies, which assume a constant friction angle, attribute this anomalously low friction angle to possibly very weak, clay-rich smear gouges in normal faults in the well region (Brown et al., 2003; Numelin et al., 2007; Suppe, 2014). Our analysis, in contrast, suggests that the low friction angle indicated by the well data results from a significant decrease of the friction angle with stress (red solid line, Figure 7a).

3.5 Stress field in a salt basin

We estimate stresses around a submarine salt body below the Sigsbee Escarpment in Mad Dog Field, deepwater Gulf of Mexico (Figure 8a). The strain and stress states of the rocks in this region can differ significantly from those developed under purely vertical, uniaxial strain because the salt body and the significant topography at the Sigsbee Escarpment significantly affect both the magnitude and the orientation of principal stresses in adjacent rocks (Fredrich et al., 2003; Heidari et al., 2017; Nikolinakou et al., 2018a). The magnitude and extent of salt and topography's effects on stresses depend on the mechanical behavior of the rocks. We use the original and stress-dependent MCC models to estimate stresses in this region and to assess the impact of the stress dependency of rock properties on estimated stresses.

We build a finite-element 2D plane-strain model of the salt basin in Abaqus (DassaultSystems, 2013) (Figure 8a). The constitutive equations of the original and new MCC models are integrated numerically using the backward Eulerian method, encoded as UMAT subroutines, and linked to the Abaqus model. Horizontal displacement is fixed at the side boundaries of the model, and vertical displacement is fixed at the bottom boundary (Figure 8a). Salt is modeled as a nearly incompressible (compressibility coefficient, κ_{salt} = 0.01) poro-elastic material with low shear stiffness (shear modulus, G = 0.01 MPa). The density of salt is 2.2 g/cm^3. The mechanical parameters of RGoM EI mudrocks are used for rocks in our model, assuming that rocks in the Mad Dog field have similar properties as those in Eugene Island, Gulf of Mexico. The density of the rocks is 2.253 g/cm^3. Pore pressure is assumed to be hydrostatic (drained analysis). The model begins with almost zero initial stresses everywhere, and then the weight of salt and sediments is applied gradually over time. Stresses are obtained after the entire weight has been applied (Nikolinakou et al., 2013).

The ratio of the least to maximum effective principal stress predicted by the original MCC model (Figure 8b) significantly differs from the value of this ratio at the uniaxial-strain condition (K_0 = 0.79; Figure 1c) in several areas around the salt body. It is lower than K_0 in sediments around the right bottom corner of the body and higher in areas below, above, and to the left of the body (Figure 8b).

The stress ratios predicted by the new MCC model (Figure 8c) are significantly different from those predicted by the original MCC model (Figure 8b). Except in shallow sediments near

the basin surface, the new MCC model predicts a higher stress ratio than the original MCC model at any given point (Figure 8c). This agrees with the fact that the friction angle at high stresses in non-shallow rocks is lower in the new MCC model (solid line, Figure 1b) than the average value used in the original model (dashed line, Figure 1b). The new MCC model does not significantly affect the distribution of the stress ratio across the basin. This is because this distribution is controlled primarily by salt and the topography of the basin surface, and the mechanical properties of the sediments have a secondary role in this distribution.

(a)

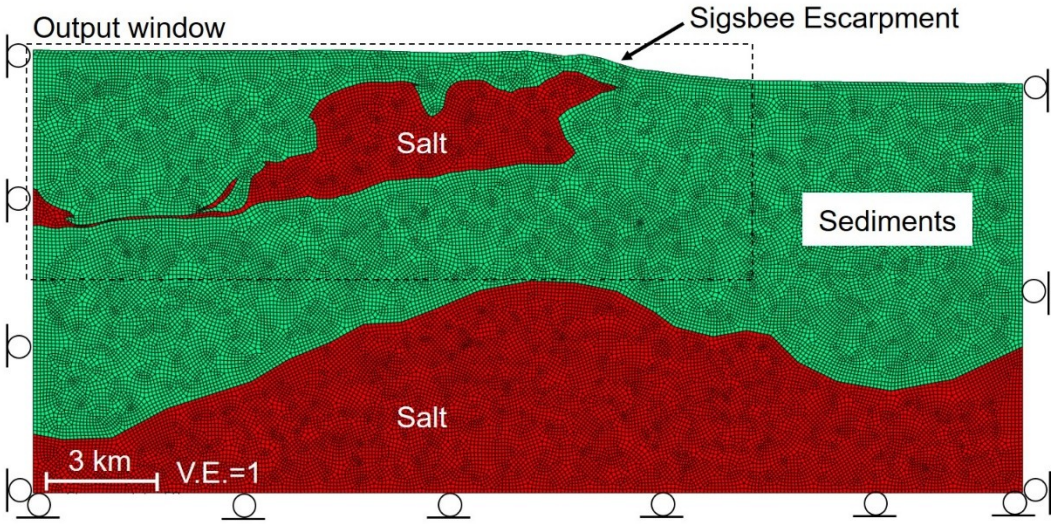

(b)

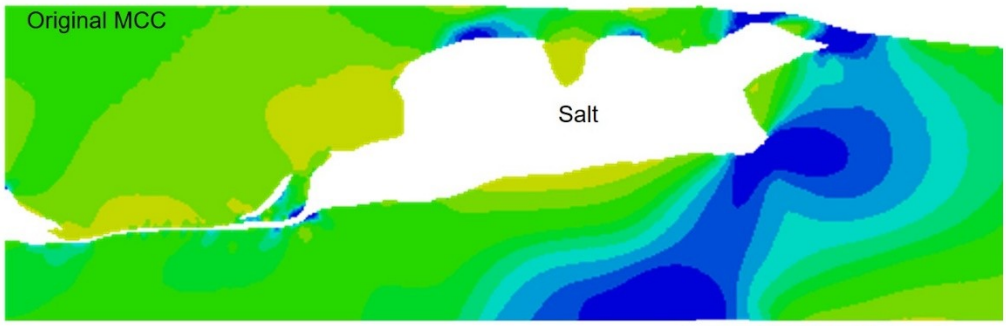

Ratio of least to maximum principal effective stress, σ'_3 / σ'_1

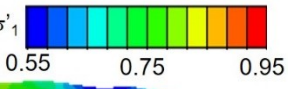

(c)

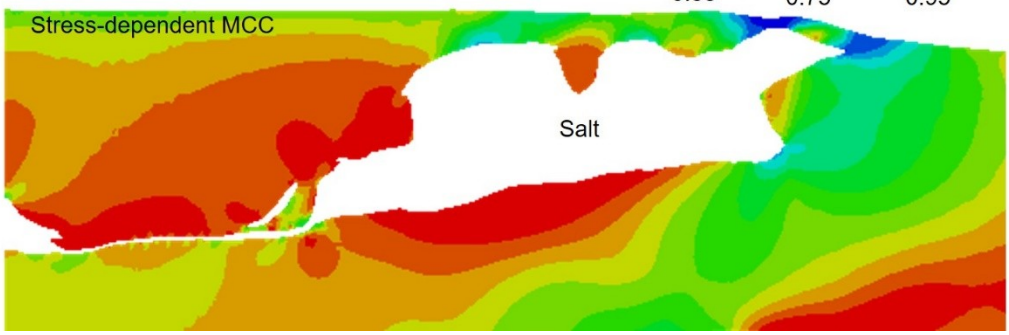

Figure 8. Plane-strain finite-element analysis of a salt basin in Mad Dog Field, deepwater Gulf of Mexico. Geometry of the salt body and seabed topography are based on seismic data provided by BP & Partners. (a) Finite-element mesh and boundary conditions. (b) Ratio of the least to maximum effective principal stress predicted by the original MCC model. (c) Ratio of the least to maximum effective principal stress predicted by the new, stress-dependent MCC model.

4 Conclusions

We modify the Modified Cam-Clay model to incorporate the decrease in the friction angle and the slope of the compression curve with stress, observed in experiments over a stress range of up to 100 MPa. With only one additional parameter, the new model successfully predicts the significant increase of the K_0 ratio and the decrease of the undrained-strength ratio with stress. We encode the new MCC model to use it in conjunction with a finite-element model of a salt basin. The new model predicts significantly different stresses around salt compared to the original MCC model.

We demonstrate the implications of the stress dependency of the friction angle for drilling wellbores, the topography of critical wedges, the stability of submarine channel levees, and the strength profile of the Earth's crust. We revisit and modify analytical models developed for these processes and show that the decrease of the friction angle with stress 1) results in a concave surface for critical wedges, 2) shifts the drilling window to higher mud weights and makes it narrower for a vertical wellbore, and 3) causes failure of submarine channel levees at lower angles.

Our study could improve estimation of stresses, pore pressure, drilling window for wellbores, and quantitative analysis of geological processes that depend on friction angle.

Acknowledgements

This study was funded by the UT GeoFluids and Applied Geodynamics Laboratory (AGL) research consortia and by the Jackson School of Geosciences at The University of Texas at Austin. AGL is supported by Anadarko, Aramco, BHP Billiton, BP, Chevron, NOOC, Condor Petroleum Inc., EcoPetrol, EMGS, Eni, ExxonMobil, Fieldwood Energy, Hess, Ion, Midland Valley, Murphy Oil Corporation, Noble Energy, BR Petrobras, Petronas, PGS, Repsol, Rockfield, Talos Energy, Shell, TGS, Spectrum, Total, and WesternGeco. UT GeoFluids is supported by Anadarko, BHP Billiton, BP, Chevron, Conoco-Phillips, ExxonMobil, Hess, Pemex, Repsol, Shell, and Statoil. Datasets for this research are included in Casey et al. (2016) and Ge (2019).

References

Abdulhadi, N. O., Germaine, J. T., and Whittle, A. J., 2012, Stress-dependent behavior of saturated clay: Canadian Geotechnical Journal, v. 49, no. 8, p. 907-916.

Alberty, M. W., and McLean, M. R., 2004, A Physical Model for Stress Cages, SPE Annual Technical Conference and Exhibition: Houston, Texas, Society of Petroleum Engineers, p. 8.

Atkinson, J. H., and Bransby, P., 1977, The mechanics of soils, an introduction to critical state soil mechanics, 0042-3114.

Bishop, A., Webb, D., and Lewin, P., 1965, Undisturbed samples of London Clay from the Ashford Common shaft: strength–effective stress relationships: Geotechnique, v. 15, no. 1, p. 1-31.

676 Bohn, C. W., IV, Flemings, P. B., and Slingerland, R. L., 2012, Accommodation Change During Bypass
677 Across a Late-Stage Fan in the Shallow Auger Basin
678 Application of the Principles of Seismic Geomorphology to Continental Slope and Base-of-Slope Systems:
679 Case Studies from SeaFloor and Near-Sea Floor Analogues, *in* Prather, B. E., Deptuck, M. E.,
680 Mohrig, D., Hoorn, B. V., and Wynn, R. B., eds., Volume 99, SEPM Society for Sedimentary
681 Geology, p. 0.
682 Breen, N. A., and Orange, D. L., 1992, The effects of fluid escape on accretionary wedges 1. Variable
683 porosity and wedge convexity: Journal of Geophysical Research: Solid Earth, v. 97, no. B6, p.
684 9265-9275.
685 Brooker, E. W., and Ireland, H. O., 1965, Earth pressures at rest related to stress history: Canadian
686 geotechnical journal, v. 2, no. 1, p. 1-15.
687 Brown, K. M., Kopf, A., Underwood, M. B., and Weinberger, J. L., 2003, Compositional and fluid pressure
688 controls on the state of stress on the Nankai subduction thrust: A weak plate boundary: Earth
689 and Planetary Science Letters, v. 214, no. 3, p. 589-603.
690 Burland, J., 1990, On the compressibility and shear strength of natural clays: Géotechnique, v. 40, no. 3,
691 p. 329-378.
692 Butterfield, R., 1979, A natural compression law for soils: Géotechnique, v. 29, no. 4, p. 469-480.
693 Casey, B., Germaine, J. T., Flemings, P. B., and Fahy, B. P., 2016, In situ stress state and strength in
694 mudrocks: Journal of Geophysical Research: Solid Earth, v. 121, no. 8, p. 5611-5623.
695 Casey, B., Reece, J., and Germaine, J., 2019, One-dimensional normal compression laws for
696 resedimented mudrocks: Marine and Petroleum Geology.
697 Cook, A. E., and Sawyer, D. E., 2015, The mud-sand crossover on marine seismic data: Geophysics, v. 80,
698 no. 6, p. A109-A114.
699 Dahlen, F., 1990, Critical taper model of fold-and-thrust belts and accretionary wedges: Annual Review
700 of Earth and Planetary Sciences, v. 18, no. 1, p. 55-99.
701 Dahlen, F., Suppe, J., and Davis, D., 1984, Mechanics of fold–and–thrust belts and accretionary wedges:
702 Cohesive Coulomb theory: Journal of Geophysical Research: Solid Earth, v. 89, no. B12, p. 10087-
703 10101.
704 DassaultSystems, 2013, Commercial finite element code Abaqus 6.13-2.
705 Davis, D., Suppe, J., and Dahlen, F. A., 1983, Mechanics of fold-and-thrust belts and accretionary
706 wedges: Journal of Geophysical Research: Solid Earth, v. 88, no. B2, p. 1153-1172.
707 Fearon, R., and Coop, M., 2000, Reconstitution: what makes an appropriate reference material?:
708 Géotechnique, v. 50, no. 4, p. 471-477.
709 Flemings, P. B., and Saffer, D. M., 2018, Pressure and Stress Prediction in the Nankai Accretionary Prism:
710 A Critical State Soil Mechanics Porosity-Based Approach: Journal of Geophysical Research: Solid
711 Earth, p. n/a-n/a.
712 Flemings, P. B., Stump, B. B., Finkbeiner, T., and Zoback, M., 2002, Flow focusing in overpressured
713 sandstones: Theory, observations, and applications: American Journal of Science, v. 302, no. 10,
714 p. 827-855.
715 Fredrich, J. T., Coblentz, D., Fossum, A. F., and Thorne, B. J., 2003, Stress perturbations adjacent to salt
716 bodies in the deepwater Gulf of Mexico, Society of Petroleum Engineers Annual Technical
717 Conference and Exhibition: Denver, Colorado, 2003. Society of Petroleum Engineers.
718 Gaines, S., Walton, G., and Labrie, D., 2019, Residual Properties Estimated from Post-Peak Triaxial
719 Unloading: Case Study of a Hard Rock Mine Site, 53rd U.S. Rock Mechanics/Geomechanics
720 Symposium: New York City, New York, American Rock Mechanics Association, p. 10.
721 Gao, B., Flemings, P. B., Nikolinakou, M. A., Saffer, D. M., and Heidari, M., 2018, Mechanics of Fold–and–
722 Thrust Belts Based on Geomechanical Modeling: Journal of Geophysical Research: Solid Earth, v.
723 0, no. 0.

724 Ge, C., 2019, Compression behavior of smectitic vs. illitic mudrocks [PhD: Massachusetts Institute of
725 Technology. Department of Civil and Environmental Engineering.
726 Gibson, R., and Morgenstern, N., 1962, A note on the stability of cuttings in normally consolidated clays:
727 Geotechnique, v. 12, no. 3, p. 212-216.
728 Goulty, N., 2004, Mechanical compaction behaviour of natural clays and implications for pore pressure
729 estimation: Petroleum Geoscience, v. 10, no. 1, p. 73-79.
730 Hart, B. S., Flemings, P. B., and Deshpande, A., 1995, Porosity and pressure: Role of compaction
731 disequilibrium in the development of geopressures in a Gulf Coast Pleistocene basin: Geology, v.
732 23, no. 1, p. 45-48.
733 Hashiguchi, K., Isotropic Hardening Theory for Granular Media, *in* Proceedings Proceedings of the Japan
734 Society of Civil Engineers1974, Volume 1974, Japan Society of Civil Engineers, p. 45-60.
735 Hashiguchi, K., 1995, On the linear relations of v–ln p and ln v–ln p for isotropic consolidation of soils:
736 International journal for numerical and analytical methods in geomechanics, v. 19, no. 5, p. 367-
737 376.
738 Hauser, M. R., Couzens-Schultz, B. A., and Chan, A. W., 2014, Estimating the influence of stress state on
739 compaction behavior: Geophysics, v. 79, no. 6, p. D389-D398.
740 Heidari, M., Nikolinakou, M. A., and Flemings, P. B., 2018a, Coupling geomechanical modeling with
741 seismic pressure prediction: GEOPHYSICS, v. 83, no. 5, p. B253-B267.
742 Heidari, M., Nikolinakou, M. A., Flemings, P. B., and Hudec, M. R., 2017, A simplified stress analysis of
743 rising salt domes: Basin Research, v. 29, no. 3, p. 363-376.
744 Heidari, M., Nikolinakou, M. A., Flemings, P. B., and Hudec, M. R., 2018b, Enhancing Modified-Cam-Clay
745 Model for Large Stress Range, 52nd U.S. Rock Mechanics/Geomechanics Symposium: Seattle,
746 Washington, American Rock Mechanics Association, p. 6.
747 Heidari, M., Nikolinakou, M. A., Hudec, M. R., and Flemings, P. B., 2019, Influence of a reservoir bed on
748 diapirism and drilling hazards near a salt diapir: a geomechanical approach: Petroleum
749 Geoscience, v. 25, no. 3, p. 282-297.
750 Holtz, R. D., and Kovacs, W. D., 1981, An introduction to geotechnical engineering, v. Monograph.
751 Hubbert, M., and Rubey, W. W., 1959, Role of fluid pressure in mechanics of overthrust faulting:
752 I.Mechanics of fluid-filled porous solids and its application to overthrust faulting: Geological
753 Society of America Bulletin, v. 70, no. 2, p. 115-166.
754 Hunter, J. H., and Schuster, R., 1968, Stability of simple cuttings in normally consolidated clays:
755 Geotechnique, v. 18, no. 3, p. 372-378.
756 Hüpers, A., Torres, M. E., Owari, S., McNeill, L. C., Dugan, B., Henstock, T. J., Milliken, K. L., Petronotis, K.
757 E., Backman, J., Bourlange, S., Chemale, F., Chen, W., Colson, T. A., Frederik, M. C. G., Guèrin, G.,
758 Hamahashi, M., House, B. M., Jeppson, T. N., Kachovich, S., Kenigsberg, A. R., Kuranaga, M.,
759 Kutterolf, S., Mitchison, F. L., Mukoyoshi, H., Nair, N., Pickering, K. T., Pouderoux, H. F. A., Shan,
760 Y., Song, I., Vannucchi, P., Vrolijk, P. J., Yang, T., and Zhao, X., 2017, Release of mineral-bound
761 water prior to subduction tied to shallow seismogenic slip off Sumatra: Science, v. 356, no. 6340,
762 p. 841-844.
763 Ikari, M. J., Saffer, D. M., and Marone, C., 2007, Effect of hydration state on the frictional properties of
764 montmorillonite–based fault gouge: Journal of Geophysical Research: Solid Earth, v. 112, no. B6.
765 Jaky, J., 1948, Pressure in silos: Proc. 2nd ICSM, 1948.
766 Jobe, Z. R., Lowe, D. R., and Uchytil, S. J., 2011, Two fundamentally different types of submarine canyons
767 along the continental margin of Equatorial Guinea: Marine and Petroleum Geology, v. 28, no. 3,
768 p. 843-860.
769 Jones, C. A., 2010, Engineering properties of resedimented Ugnu clay from the Alaskan north slope:
770 Massachusetts Institute of Technology.
771 Kearey, P., Klepeis, K. A., and Vine, F. J., 2009, Global tectonics, John Wiley & Sons.

772 Kirsch, C., 1898, Die theorie der elastizitat und die bedurfnisse der festigkeitslehre: Zeitschrift des
773 Vereines Deutscher Ingenieure, v. 42, p. 797-807.
774 Kopp, H., Hindle, D., Klaeschen, D., Oncken, O., Reichert, C., and Scholl, D., 2009, Anatomy of the
775 western Java plate interface from depth-migrated seismic images: Earth and Planetary Science
776 Letters, v. 288, no. 3, p. 399-407.
777 Liu, M., and Carter, J., 2002, A structured Cam Clay model: Canadian Geotechnical Journal, v. 39, no. 6,
778 p. 1313-1332.
779 Mayne, P. W., and Kulhawy, F. H., 1982, Ko- OCR Relationships in Soil: Journal of the Soil Mechanics and
780 Foundations Division, v. 108, no. 6, p. 851-872.
781 McDowell, G., and Hau, K., 2003, A simple non-associated three surface kinematic hardening model:
782 Géotechnique, v. 53, no. 4, p. 433-437.
783 Mesri, G., and Hayat, T., 1993, The coefficient of earth pressure at rest: Canadian Geotechnical Journal,
784 v. 30, no. 4, p. 647-666.
785 Mesri, G., and Olson, R. E., 1971, Consolidation characteristics of montmorillonite: Geotechnique, v. 21,
786 no. 4, p. 341-352.
787 Moore, D. E., and Lockner, D. A., 2007, Friction of the smectite clay montmorillonite: The seismogenic
788 zone of subduction thrust faults, p. 317-345.
789 Moore, J. C., and Vrolijk, P., 1992, Fluids in accretionary prisms: Reviews of Geophysics, v. 30, no. 2, p.
790 113-135.
791 Muir Wood, D., 1990, Soil Behaviour and Critical State Soil Mechanics, Cambridge, U.K., Cambridge
792 University Press, 462 p.:
793 Nguyen, L. D., Fatahi, B., and Khabbaz, H., 2014, A constitutive model for cemented clays capturing
794 cementation degradation: International Journal of Plasticity, v. 56, p. 1-18.
795 Nikolinakou, M. A., Flemings, P. B., Heidari, M., and Hudec, M. R., 2018a, Stress and Pore Pressure in
796 Mudrocks Bounding Salt Systems: Rock Mechanics and Rock Engineering.
797 Nikolinakou, M. A., Heidari, M., Flemings, P. B., and Hudec, M. R., 2018b, Geomechanical modeling of
798 pore pressure in evolving salt systems: Marine and Petroleum Geology, v. 93, p. 272-286.
799 Nikolinakou, M. A., Merrell, M. P., Luo, G., B., F. P., and Hudec, M. R., 2013, Geomechanical modeling of
800 the Mad Dog salt, Gulf of Mexico, 47th US Rock Mechanics Symposium: San Francisco, CA, 23-26
801 June, 2013.
802 Numelin, T., Marone, C., and Kirby, E., 2007, Frictional properties of natural fault gouge from a low-angle
803 normal fault, Panamint Valley, California: Tectonics, v. 26, no. 2.
804 Pestana, J. M., and Whittle, A., 1995, Compression model for cohesionless soils: Géotechnique, v. 45, no.
805 4, p. 611-631.
806 Roscoe, K. H., and Burland, J. B., 1968, On the generalized stress-strain behaviour of "wet" clay, *in*
807 Heyman, J., ed., Engineering Plasticity: Cambridge, England, Cambridge University Press, p. 535-
808 609.
809 Rouainia, M., and Muir Wood, D., 2000, A kinematic hardening constitutive model for natural clays with
810 loss of structure: Géotechnique, v. 50, no. 2, p. 153-164.
811 Saffer, D. M., and Marone, C., 2003, Comparison of smectite-and illite-rich gouge frictional properties:
812 application to the updip limit of the seismogenic zone along subduction megathrusts: Earth and
813 Planetary Science Letters, v. 215, no. 1-2, p. 219-235.
814 Saffer, D. M., and Tobin, H. J., 2011, Hydrogeology and Mechanics of Subduction Zone Forearcs: Fluid
815 Flow and Pore Pressure: Annual Review of Earth and Planetary Sciences, v. 39, no. 1, p. 157-186.
816 Sawyer, D. E., Flemings, P. B., and Nikolinakou, M., 2014, Continuous deep-seated slope failure recycles
817 sediments and limits levee height in submarine channels: Geology, v. 42, no. 1, p. 15-18.

Screaton, E., and Ge, S., 2000, Anomalously high porosities in the proto–decollement zone of the Barbados Accretionary Complex: Do they indicate overpressures?: Geophysical research letters, v. 27, no. 13, p. 1993-1996.
Skarbek, R. M., and Rempel, A. W., 2017, Heterogeneous Coulomb wedges: Influence of fluid pressure, porosity, and application to the Hikurangi subduction margin, New Zealand: Journal of Geophysical Research: Solid Earth, v. 122, no. 3, p. 1585-1613.
Stern, R. J., 2002, Subduction zones: Reviews of geophysics, v. 40, no. 4, p. 3-1-3-38.
Stigall, J., and Dugan, B., 2010, Overpressure and earthquake initiated slope failure in the Ursa region, northern Gulf of Mexico: Journal of Geophysical Research: Solid Earth, v. 115, no. B4.
Suebsuk, J., Horpibulsuk, S., and Liu, M. D., 2010, Modified Structured Cam Clay: A generalised critical state model for destructured, naturally structured and artificially structured clays: Computers and Geotechnics, v. 37, no. 7-8, p. 956-968.
Suppe, J., 2007, Absolute fault and crustal strength from wedge tapers: Geology, v. 35, no. 12, p. 1127-1130.
Suppe, J., 2014, Fluid overpressures and strength of the sedimentary upper crust: Journal of Structural Geology, v. 69, p. 481-492.
Velde, B., 1996, Compaction trends of clay-rich deep sea sediments: Marine Geology, v. 133, no. 3, p. 193-201.
Whittle, A. J., and Kavvadas, M. J., 1994, Formulation of MIT-E3 constitutive model for overconsolidated clays: Journal of Geotechnical Engineering, v. 120, no. 1, p. 173-198.
Willson, S. M., and Fredrich, J. T., 2005, Geomechanics considerations for through- and near-salt well design, SPE Annual Technical Conference and Exhibition: Dallas, Texas, Society of Petroleum Engineers, p. 1-17.
Winker, C. D., and Shipp, R. C., 2002, Sequence Stratigraphic Framework for Prediction of Shallow Water Flow in the Greater Mars-Ursa Area, Mississippi Canyon Area, Gulf of Mexico Continental Slope Sequence Stratigraphic Models for Exploration and Production: Evolving Methodology, Emerging Models and Application Histories, *in* Armentrout, J. M., and Rosen, N. C., eds., Volume 22, SEPM Society for Sedimentary Geology, p. 0.
Xiao, H. B., Dahlen, F., and Suppe, J., 1991, Mechanics of extensional wedges: Journal of Geophysical Research: Solid Earth, v. 96, no. B6, p. 10301-10318.
Yassir, N. A., 1989, Mud volcanoes and the behaviour of overpressured clays and silts: University of London.
Zhao, W. L., Davis, D., Dahlen, F., and Suppe, J., 1986, Origin of convex accretionary wedges: Evidence from Barbados: Journal of Geophysical Research: Solid Earth, v. 91, no. B10, p. 10246-10258.
Zoback, M. D., 2010, Reservoir Geomechanics, Cambridge University Press.
Zoback, M. D., Apel, R., Baumgärtner, J., Brudy, M., Emmermann, R., Engeser, B., Fuchs, K., Kessels, W., Rischmüller, H., and Rummel, F., 1993, Upper-crustal strength inferred from stress measurements to 6 km depth in the KTB borehole: Nature, v. 365, no. 6447, p. 633.